pubs.acs.org/iacsau

Structural, Ionic, and Electronic Properties of Solid-State Phthalimide-Containing Polymers for All-Organic Batteries

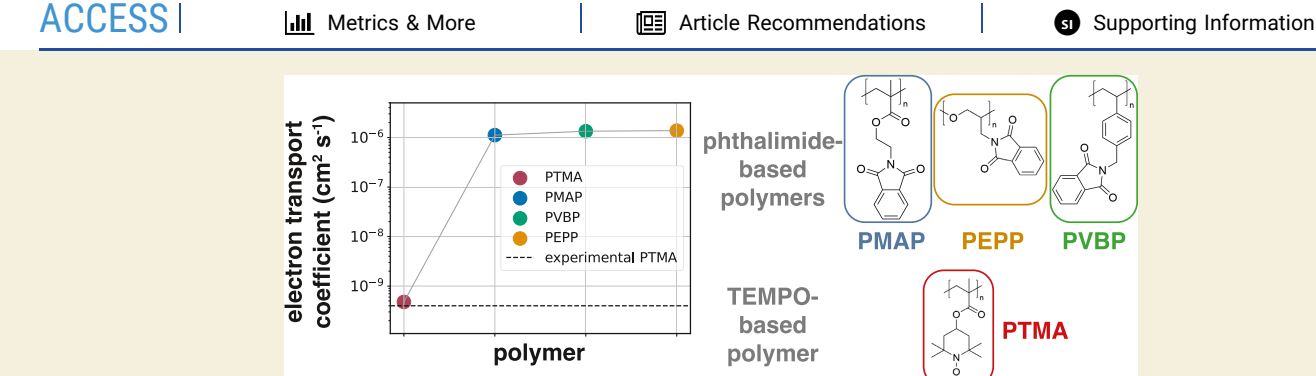
Riccardo Alessandri, Cheng-Han Li, Sheila Keating, Khirabdhi T. Mohanty, Aaron Peng, Jodie L. Lutkenhaus, Stuart J. Rowan, Daniel P. Tabor,* and Juan J. de Pablo*



Downloaded via TEXAS A&M UNIV COLG STATION on September 27, 2024 at 19:52:16 (UTC). See https://pubs.acs.org/sharingguidelines for options on how to legitimately share published articles.

Cite This: JACS Au 2024, 4, 2300-2311





ABSTRACT: Redox-active polymers serving as the active materials in solid-state electrodes offer a promising path toward realizing all-organic batteries. While both cathodic and anodic redox-active polymers are needed, the diversity of the available anodic materials is limited. Here, we predict solid-state structural, ionic, and electronic properties of anodic, phthalimide-containing polymers using a multiscale approach that combines atomistic molecular dynamics, electronic structure calculations, and machine learning surrogate models. Importantly, by combining information from each of these scales, we are able to bridge the gap between bottom-up molecular characteristics and macroscopic properties such as apparent diffusion coefficients of electron transport (D_{app}) . We investigate the impact of different polymer backbones and of two critical factors during battery operation: state of charge and polymer swelling. Our findings reveal that the state of charge significantly influences solid-state packing and the thermophysical properties of the polymers, which, in turn, affect ionic and electronic transport. A combination of molecular-level properties (such as the reorganization energy) and condensed-phase properties (such as effective electron hopping distances) determine the predicted ranking of electron transport capabilities of the polymers. We predict $D_{\rm app}$ for the phthalimide-based polymers and for a reference nitroxide radical-based polymer, finding a 3 orders of magnitude increase in $D_{\rm app}$ ($\approx 10^{-6}$ cm² s⁻¹) with respect to the reference. This study underscores the promise of phthalimide-containing polymers as highly capable redox-active polymers for anodic materials in all-organic batteries, due to their exceptional predicted electron transport capabilities.

KEYWORDS: redox-active polymers, multiscale modeling, all-organic batteries, molecular dynamics, organic mixed conductors

1. INTRODUCTION

Nonconjugated, redox-active polymers (RAPs) have emerged as a new class of electroactive materials. 1-3 Due to their redox, magnetic, and charge conduction properties, RAPs can be applied for a broad range of applications from optoelectronics and spintronics to memory or energy storage. 1-6 Particularly interesting is the use of RAPs as alternatives to metal-based materials for batteries. ^{1,3,7-9} In this context, RAPs may offer more flexibility for chemical degradation strategies that would enable the realization of "circular" batteries. 10,11 Moreover, allorganic batteries would offer a pathway away from the reliance of current battery technologies on metals such as lithium, nickel, and cobalt that present economic, ethical, and environmental challenges. 11,12 A key hindrance in the development of RAP-based, solid-state, all-organic batteries is that the vast majority of solid-state applications using RAPs reported to

date have relied on preferentially oxidized (i.e., p-type or highpotential) radical groups. 13,14 However, preferentially reduced (i.e., n-type or low-potential) RAPs are required as active materials for the anode. Hence, developing n-type RAPs is crucial for realizing the promise of RAPs in applications such as all-organic batteries.

RAPs are, in principle, highly modular materials, and at the most fundamental level, their redox-active group governs their

Received: March 27, 2024 Revised: May 13, 2024 Accepted: May 17, 2024 Published: June 7, 2024





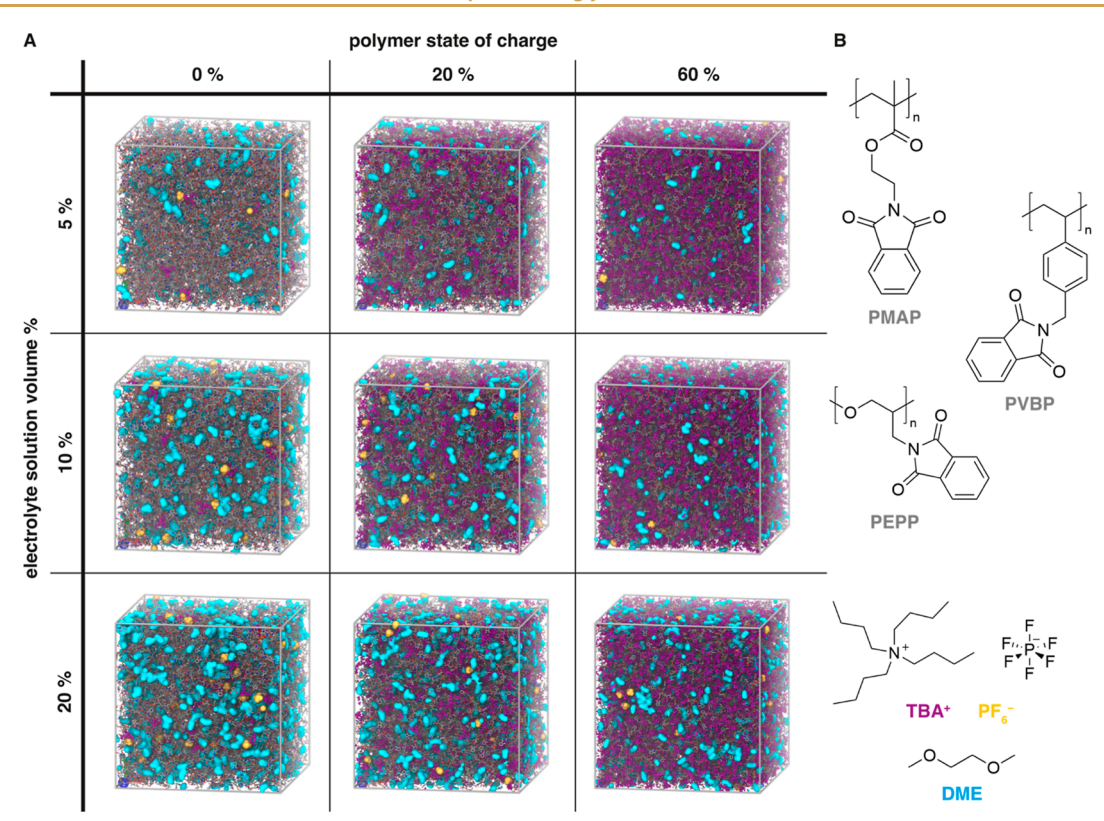


Figure 1. Systems modeled: phthalimide-based polymers at different swelling conditions and states of charge. (A) Renderings of the PMAP systems for the different swelling conditions (expressed as the electrolyte solution volume %; 5, 10, and 20%) and polymer state of charge (0, 20, and 60%) investigated. (B) Chemical structures of the components: the polymers [PMAP, PEPP, and PVBP; in gray in the renderings in panel (A)], TBA⁺ (purple), PF₆ (yellow), and DME (cyan).

electronic properties while their backbone shapes their thermophysical properties. While numerous n-type redoxactive groups have been used as molecules or dissolved oligomers in redox flow batteries, the diversity of n-type molecules appended to polymers and used in RAP-based batteries is primarily limited to viologen, quinone, or diimide species. 2,9,12,15,16 Regarding backbones, a key finding has been that flexible macromolecular backbones with near-room temperature glass-transition temperature (T_{σ}) may promote electrical conductivity by allowing for thermal annealing treatments that lead to the formation of electronically percolating networks of redox-active sites.¹⁷ This was the case for the p-type, TEMPO-based (2,2,6,6-tetramethyl-1-piperidinyloxy-based) polymer PTEO.¹⁷ Due to its poly-(ethylene oxide) backbone, it achieved a record-high electrical conductivity of 0.2 S/cm over length scales of <600 nm. 17 A similar strategy applied to the galvinoxyl n-type redox group and employing a low- T_g polysiloxane backbone also favored electrical conductivity, although the bulkiness of the galvinoxyl groups likely limited the achievable conductivity to a still relatively high value of 10⁻² S/cm. 14 Overall, understanding how the backbone-redox group design at the molecular scale translates to the polymeric material properties remains challenging.

The use of RAPs as active materials for battery electrodes, as well as for any other application involving polymer interaction with an electrolyte (such as electrochromics and sensors), is enabled by their mixed ionic-electronic conduction properties. ^{18,19} During charging, when an active material in the p-type positive electrode (n-type negative electrode) is oxidized (reduced), the redox active unit transfers (receives) an electron

from the current collector, resulting in a positively (negatively) charged species. Simultaneously, anions (cations) "dope" the polymer at the p-type positive electrode (n-type negative electrode) to maintain charge neutrality. Upon discharge, the polymer is dedoped, and the neutral redox-active unit is restored. Hence, the polymer state of charge changes during battery operation, while the polymer also "swells" due to the uptake of ions (that most often takes place together with some amount of solvent²⁰). Meanwhile, electron transfer within the RAP occurs by an electron-hopping mechanism, whereby electrons propagate homogeneously by self-exchange. 1,21,22 It remains poorly understood what the impact of the polymer state of charge and polymer swelling are on electronic and ionic properties of RAPs, and how the dry-polymer backboneredox group designs can be translated to electrolyte-rich environments.

While molecular modeling may help in our understanding of RAPs, studies have been limited, in particular in the case of n-type RAPs. Beyond TEMPO-based systems, ^{17,23-25} a generic coarse-grained model has been developed to study charge transport in RAP solutions. ²⁶ To be predictive and distinguish between the performance of various polymers, these models necessitate detailed molecular-level information regarding the particular redox-active group as their input. Another type of effort has concentrated on molecule-specific characteristics by exploring various sets of redox-active units ²⁷⁻²⁹ or oligomers ³⁰ using electronic structure methods in the gas phase. A limitation of these studies is that they do not account for condensed-phase conditions, which could potentially alter the resulting electronic properties. In summary, there is a need for chemistry-specific computational studies that address the

complex interplay between the solid-state organization of RAPs and their ionic and electronic properties.

Here, we model solid-state structural, ionic, and electronic properties of n-type, phthalimide-containing RAPs using a combination of atomistic molecular dynamics, electronic structure calculations, and machine learning surrogate models. We choose N-methyl-phthalimide, or simply phthalimide, as the redox-active group as it emerged from a recent virtual screening campaign performed by some of us as a promising group to reach both the low redox potential needed for an ntype material and the high electronic couplings needed for high electronic conductivity.²⁸ We attach phthalimide to several polymer backbones and probe how these modulate the polymer solid-state properties. We also determine the impact of two critical system parameters during battery operation, namely, the polymer state of charge and the swelling of the polymer in response to the uptake of electrolyte solution. We find that the polymer state of charge has a large impact on all properties and in a somewhat universal way across the different polymers, lowering the systems' $T_{\rm g}$ and modulating phthalimide-phthalimide configurations and thereby impacting ionic and electronic transport. Differences though emerge between the different polymers, wherein molecular-level properties (electronic couplings, reorganization energy) and condensedphase properties (density of radical sites, effective electron hopping distances) interplay to determine the electron transport properties of the polymers. While the poly(ethylene oxide)-based polymer shows the largest predicted electron transport capabilities by achieving a balance between electronic coupling strength, reorganization energy, and effective distance for electron transfer, the investigated phthalimide-containing polymers are overall very promising, possessing very high predicted diffusion coefficients of electron transfer on the order of 10^{-6} cm² s⁻¹.

2. RESULTS AND DISCUSSION

2.1. Polymer-Electrolyte-Solvent Systems

The phthalimide-based polymers of interest for this work, with different backbones, and in different states of charge and swelling conditions, are schematically shown in Figure 1. We choose to investigate different backbones because their different segmental dynamics and size may lead to different structural (e.g., phthalimide packing), ionic (e.g., ion transport), and electronic (e.g., charge percolative networks) properties of the resulting phthalimide-containing polymers. In particular, we compare poly(methyl methacrylate)-, poly-(ethylene oxide)-, and polystyrene-based polymers—poly(N-(methacryloxyethyl) phthalimide) (PMAP), poly(2,3-epoxypropylphthalimide) (PEPP), and poly(N-(vinylbenzyl) phthalimide) (PVBP), respectively—as shown in Figure 1B. Each periodic system contains 100 chains with a degree of polymerization of 30, corresponding to molecular weights of ca. 7.8, 6.1, and 7.9 kDa for PMAP, PEPP, and PVBP, respectively.

We investigate the impact of two critical system parameters—(1) state of charge and (2) swelling %—by varying them in a discrete fashion as shown in Figure 1A. During battery operation, a polymer constituting a solid-state electrode changes its state of charge or redox state. In the specific case of phthalimide-based systems, the low redox potential of this unit means that the material will be reduced. We model the neutral systems (i.e., state of charge = 0%) by having all the

phthalimide-based monomers being neutral. We model the charged systems as follows: each of the 100 chains has the same amount of charge (e.g., in the 20%-charged systems, 6 monomers out of the 30 have a charge of -1, leading to a charge of -6 per chain), with charged and uncharged monomers randomly distributed for each chain (see Methods for details). The resulting net negative charge of the charged polymers is compensated by the inclusion of TBA⁺ cations. We simulate a range of swellings that is typical of experimental settings, namely, 5, 10, and 20% (expressed as the electrolyte solution volume %).31 We model swelling by including a volume % of electrolyte solution, namely a solution of 1,2dimethoxyethane (DME) with 0.5 M of the organic salt TBAPF₆ (tetrabutylammonium hexafluorophosphate), that is equal to 5, 10, or 20% of the total simulation box volume. For more details on this procedure, and the detailed molecular composition of all systems, see Table S1 and associated discussion. Once set up, all systems are equilibrated in their melt state (at 900 K) and then cooled down to various temperatures for analysis (see Methods for details). A schematic of the overall simulation protocol is given in Figure

2.2. Glass-Transition Temperatures

First, we probe the effect of swelling and state of charge on the $T_{\rm g}$ of the polymers. We note that while the absolute value of the simulated $T_{\rm g}$ is higher than the corresponding experimental values due to the fast cooling rates used in the simulations, the atomistic force field recapitulates the ranking of $T_{\rm g}$ values observed experimentally for the bare-backbone polymers PEO < PS < PMMA (Figure S2).

Figure 2 shows how $T_{\rm g}$ varies with increasing swelling of the polymer film and at different states of charge, for PMAP. We

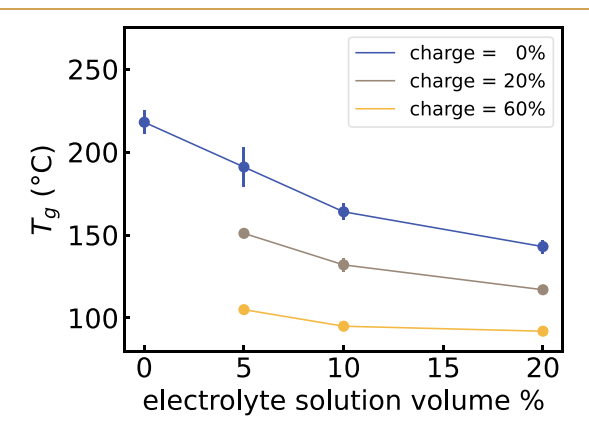


Figure 2. Computed $T_{\rm g}$ as a function of polymer swelling and state of charge. Data shown are for PMAP. Similar trends are observed for PEPP and PVBP (Figure S1). Polymer swelling is expressed as the electrolyte solution volume %. Lines connect the simulated points.

find that $T_{\rm g}$ decreases with increasing swelling of the polymer film. The decrease in $T_{\rm g}$ is expected as the swelling introduces (mainly) solvent molecules, which act as plasticizers. Figure 2 also shows that $T_{\rm g}$ decreases as the polymer gets charged. In this case, it is the TBA+ counterions that act as plasticizers. The $T_{\rm g}$ decrease caused by swelling is more marked for the uncharged polymers than for the charged ones—this is due to the fact that $T_{\rm g}$ for the charged polymer is already considerably lowered by the plasticizing effects of the TBA+ counterions. The same trends are found for the other polymers and are

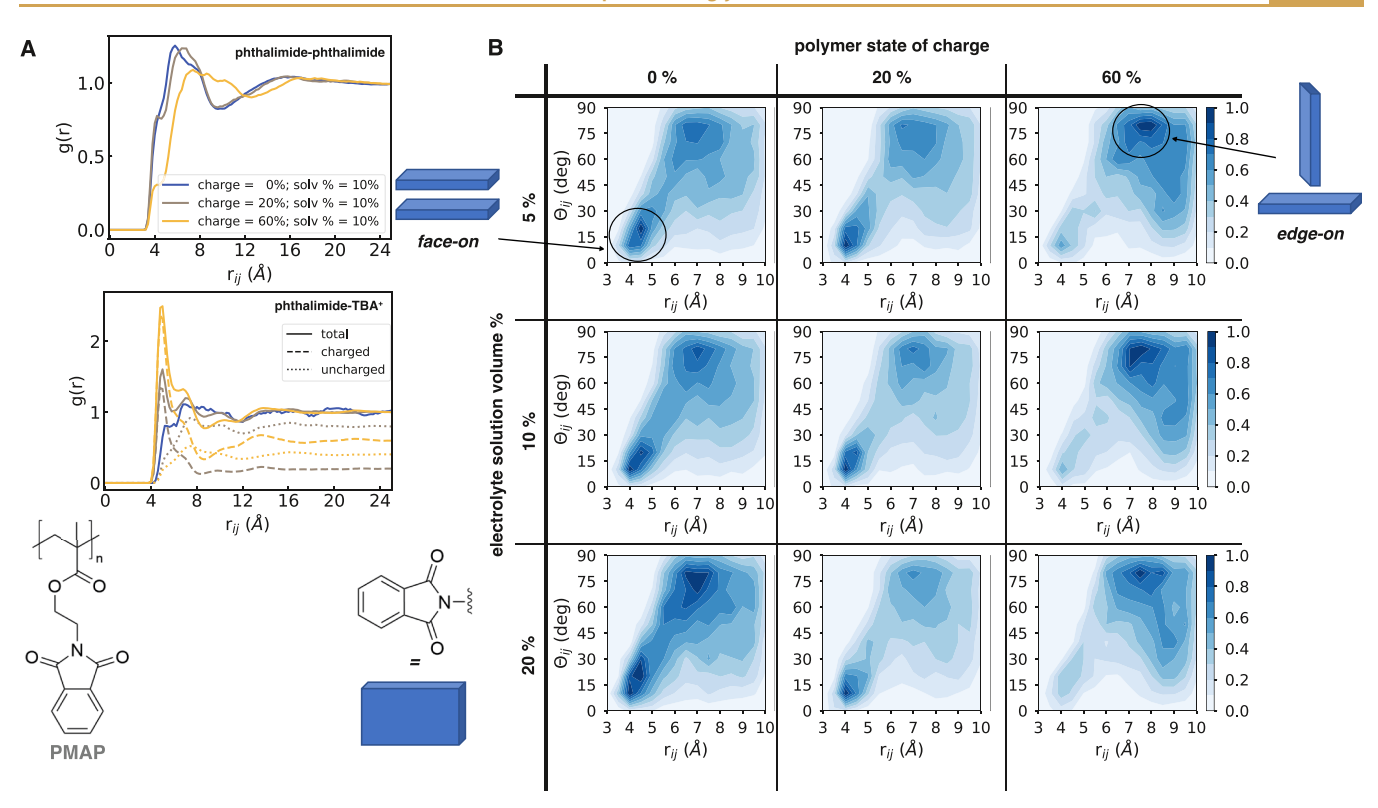


Figure 3. Structural characterization of the poly(methyl methacrylate)-based polymer. (A) RDFs between the centroids of phthalimide units (top) and between phthalimides and TBA⁺ ions (bottom); the dashed and dotted lines show the fraction of the RDF due to the *charged* and *uncharged* phthalimides, respectively. (B) Phthalimide pair configurational maps obtained by partitioning the pairs of a given condensed-phase in the two-dimensional space defined by the distance between two phthalimide units, r_{ij} , and the angle between the vectors normal to the phthalimide planes, θ_{ij} . Only pairs with $r_{ij} \leq 10$ Å were considered. $T = 1.2 \times T_g$.

shown in Figure S1. In summary, for all polymers, $T_{\rm g}$ decreases with both increased swelling and increased state of charge.

2.3. Structural Characterization

We next analyze structural properties of the different polymers, first as a function of swelling, then as a function of state of charge. To mitigate the effects of different values of $T_{\rm g}$ (Figure 2) on the structural analysis of the different polymer systems, we perform the structural characterization at the temperatures $T=0.8\times T_{\rm g}$ and $T=1.2\times T_{\rm g}$. Since the findings from the $T=1.2\times T_{\rm g}$ and $T=0.8\times T_{\rm g}$ simulations are very similar, we will only discuss the structural characterization at $T=1.2\times T_{\rm g}$ in the main text, and the $T=0.8\times T_{\rm g}$ data can be found in the Supporting Information.

We first note that swelling has a negligible effect on the structure of the polymers as characterized by radial distribution functions (RDFs) (Figure S5). In particular, we look at the RDF between (the centroids of) phthalimide units, which gives us insights into phthalimide packing, and the RDF between (the centroids of) phthalimide units and TBA+ counterions, which informs us on the location of counterions with respect to the redox centers. The negligible impact of swelling on the polymer structures, as probed via the RDFs, applies to all polymers (Figure S5). We conclude that these polymers are structurally robust to the uptake of electrolyte solution, that is, we observe no structural changes such as different packing motifs for the phthalimides, for the swellings of up to 20% electrolyte solution volume investigated here.

We next examine the same RDFs but now as a function of state of charge of the polymer. The phthalimide—phthalimide RDF in Figure 3A shows that, as the polymer goes to higher

states of charge, there is a decrease in the first RDF peak at around 4 Å and a decrease (and shift toward larger distances) of the second RDF peak at around 7–8 Å between 20 and 60% state of charge. These decreases indicate a reduction in phthalimide—phthalimide interactions upon polymer charging. Simultaneously, there is a drastic increase in the first phthalimide—TBA+ RDF peak (Figure 3A, bottom), indicating an increase in phthalimide—TBA+ interactions upon polymer charging.

By analyzing the contributions to this RDF due to charged and uncharged PMAP monomers, we can see that the drastic increase in the first phthalimide-TBA+ RDF peak is almost entirely due to charged phthalimide-TBA+ interactions (dashed lines in Figure 3A), as could be anticipated. The effect of the change of state of charge on the structure that we just described for PMAP is very similar also in the case of PEPP and PVBP (see Figure S7), with the drastic change again happening between state of charge 20 and 60%. The only qualitative difference between the polymers is the significantly smaller increase in phthalimide-TBA+ interactions in the case of PEPP (Figure S7). The reduced interactions are due to the more limited space between phthalimides available to accommodate TBA+ ions, caused by the shorter backbonephthalimide linker of PEPP with respect to PMAP and PVBP. Finally, in terms of the overall phthalimide-phthalimide RDF features, PEPP is qualitatively different from PMAP and PVBP (Figure S7), as discussed more in detail in the section below.

To get a better understanding of the solid-state packing underlying the RDFs as shown in Figure 3A, we analyze phthalimide—phthalimide pair configurations. We consider all the phthalimide—phthalimide pairs that are within a $r_{ii} = 10 \text{ Å}$

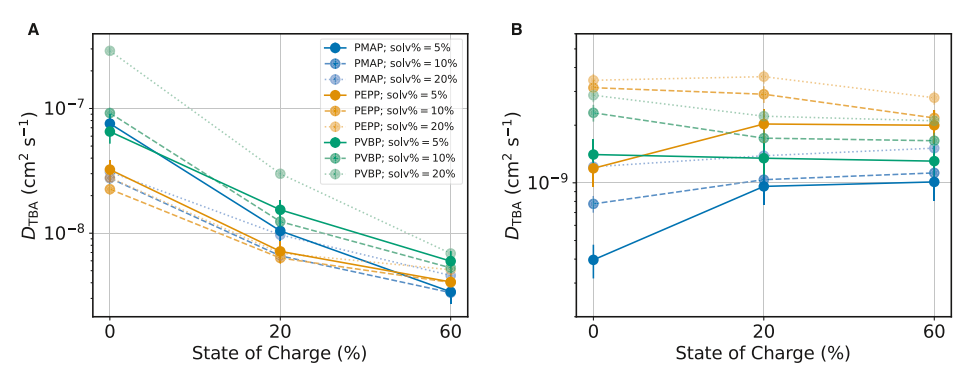


Figure 4. TBA⁺ ion diffusion coefficient, D_{TBA} , as a function of state of charge and swelling for the different polymers. (A) $T = 1.2 \times T_{\text{g}}$ and (B) T = 300 K. The values of D_{TBA} are obtained using the Einstein relation from the mean squared displacement of TBA⁺ ions.

cutoff distance, where i and j are the indices of two phthalimide units and r_{ij} is the distance between their centroids. We subsequently compute other geometrical descriptors for such pairs, such as the angle between the vectors normal to the phthalimide planes, θ_{ij} , and obtain two-dimensional maps such as the ones shown in Figure 3B (see Methods for further details). Such maps allow us to distinguish between different phthalimide packings, such as face-on $(r_{ij} \approx 4 \text{ Å} \text{ and } 0 \leq \theta_{ij} \leq 25^{\circ})$ and edge-on $(r_{ij} > 6 \text{ Å} \text{ and } 65 \leq \theta_{ij} \leq 90^{\circ})$ stacking configurations, schematically shown in Figure 3B.

Figure 3B shows how configurational maps change as a function of swelling and polymer state of charge, for PMAP. First of all, the maps show how the peak around 4 Å in the phthalimide-phthalimide RDF of Figure 3A is due to face-on configurations, while the second peak is dominated by edge-on configurations. Moreover, the key observation that emerges from the maps is the almost complete disappearance of face-on configurations when going from a state of charge of 20 to 60%. This is consistent with, and sheds more light on, the RDF results previously discussed. Similar trends are observed for PEPP (Figure S9) and PVBP (Figure S10). However, PEPP shows a lower amount of face-on configurations to begin with, which explains the qualitative difference in the RDFs noted earlier. To summarize the findings from the configurational maps, the phthalimide orientational packing goes from face-on dominated to edge-on dominated as the polymers become more highly charged.

A final aspect of interest that we can probe from a structural point of view is whether phthalimide-phthalimide pairs are predominantly intra- or inter-polymer chain. Figure S12 shows that pairs are predominantly interchain, with such pairs constituting approximately 75, 70, and 70% of the total number of pairs in the case of PMAP, PEPP, and PVBP, respectively (at 5% swelling). Swelling again has an almost negligible impact, while the polymer state of charge reduces the amount of interchain pairs, especially so in the case of PEPP. At 60% charge, interchain pairs constitute approximately 65, 48, and 60% of the total number of pairs in the case of PMAP, PEPP, and PVBP, respectively. This is consistent with the fact that, due to TBA+ intercalation upon polymer charging, the spacing between polymer chains is expected to increase, thereby decreasing the likelihood of interchain pairs. In summary, the structural characterization shows that, upon polymer charging, TBA+ counterions interact with charged phthalimide units and by doing so disrupt face-on stacking between phthalimides.

2.4. Ionic Diffusivity

To provide insights into the ionic properties of this class of organic mixed ionic-electronic conductors, we next investigate ion diffusivity in our systems. To assess ion diffusion, we examine the mean squared displacement of TBA⁺. We note that these ions do not reach the diffusive regime over the time interval over which we computed the mean squared displacement (see Figure S14). However, we can assess trends between the different systems and gather insights on the effect that state of charge, swelling, and polymer backbone have on ion diffusivity by extracting diffusion coefficients for the longest simulated times

Figure 4 shows the diffusion coefficients of TBA⁺, D_{TBA} , computed from the ion mean squared displacement using the Einstein relation (see also Figure S14), for the different polymers at different states of charge. To mitigate the effects of different T_g 's (Figure 2), we first examine the behavior of the diffusion coefficients at $T = 1.2 \times T_g$ (Figure 4A). The three polymers all show a decrease in D_{TBA} by approximately 1 order of magnitude when their state of charge increases from 0 to 60%. We ascribe this to increased electrostatic interactions that slow down ion diffusion. Differences between the three polymers are minor, with PMAP and PVBP showing somewhat larger D_{TBA} values, which we ascribe to the higher temperatures (because of the higher $T_{\rm g}$ of these systems with respect to PEPP, Figure S1). In the Supporting Information, Figure S13, we plot D_{TBA} as a function of distance from T_{g} [in particular, $1000/(T-T_g)$] for the various systems. Consistently with Figure 4A, the plot shows that D_{TBA} coefficients generally increase with increasing swelling %, while they decrease with increasing state of charge.

We now also examine TBA⁺ diffusion coefficients at $T=300~\rm K$ (Figure 4B), as these diffusion coefficients are expected to correlate with experimental ionic diffusivity during battery operation at room temperature. On Figure 4B, PEPP shows the largest TBA⁺ diffusion coefficients overall, reflecting PEPP's backbone higher segmental mobility. The behavior of $D_{\rm TBA}$ at $T=300~\rm K$ as a function of state of charge and swelling can be explained in terms of lowering of the systems' $T_{\rm g}$. Overall, the poly(ethylene oxide) backbone provides the largest ion diffusion coefficients among the investigated phthalimide-containing polymers at room temperature, with $T_{\rm g}$ of the systems overall controlling TBA^+ diffusivity.

2.5. Electronic Couplings

We now connect the larger length scales sampled by atomistic molecular dynamics (solid-state packing) to the molecularlevel electronic picture, a connection that is lacking in the

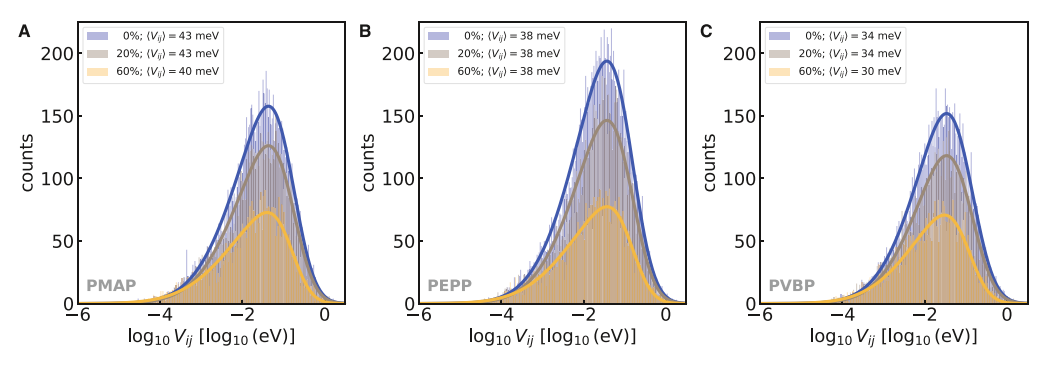


Figure 5. Electronic coupling distributions as a function of state of charge for the different polymers. (A) PMAP, (B) PEPP, and (C) PVBP. Mean electronic couplings, $\langle V_{ij} \rangle$, obtained as the mode of the skew Gaussian distribution fits, are reported in the legends. Electrolyte solution volume % = 10%. T = 300 K.

literature for this class of polymers with redox-active units other than TEMPO. In particular, we start from evaluating electronic couplings between phthalimide pairs. The electronic coupling has a strong impact on the kinetics of charge transport in these systems, which as mentioned above, generally transport via a charge-hopping mechanism. ^{1,21,22} Such electronic couplings are greatly affected by the solid-state packing of the redox-active units.

Each of our condensed-phase systems contains between 5 \times 10^3 and 13×10^3 phthalimide pairs that are within a 10 Å r_{ii} cutoff distance. To make the computation of electronic couplings for many such condensed-phase systems feasible, we use two approximations. First, we approximate the strength of the electronic coupling through evaluating orbital overlaps between the two molecules in the pair. This approximation, that is widely applied in the field for organic semiconductors, ³² holds well also for these phthalimide-based polymers studied in this work, as can be seen by the linear correlation that we find between orbital overlaps and DIPRO (DImer PROjection)³³ electronic couplings (see Methods for details) shown in Figure S16. A similar correlation between orbital overlaps and electronic couplings between redox-active groups has also been recently observed in ref 30. Second, we trained an artificial neural network as a surrogate model for orbital overlap calculations, achieving good accuracy ($R^2 = 0.83 - 0.92$, Figure S17; with distribution means predicted with very good accuracy, Figure S18), and in this way further increasing the throughput. For details on the data set construction and training, see Methods.

Figure 5 shows how the distribution of electronic couplings changes as a function of polymer state of charge. For all polymers, we observe that (1) there is a clear decrease in total number of pairs within the 10 Å r_{ij} cutoff distance when going from 0 to 20 to 60% state of charge, (2) the peak of the distribution remains constant between 0 and 20% for all polymers, while (3) it shifts by 3-4 meV lower couplings between 20 and 60% for PMAP and PVBP but not for PEPP, suggesting a higher robustness of PEPP's couplings to changes in state of charge, which we ascribe to the lower amount of face-on configurations observed earlier, and (3) PMAP shows the largest couplings, followed by PEPP and then PVBP. Together with the RDF results, these results show how the significant decreases in face-on configurations at 60% state of charge lead to a significant shift of the electronic coupling distribution that is likely detrimental to electron transport.

Another difference between the polymers that emerges from Figure 5 is the greater absolute number of pairs found for

PEPP within the given cutoff distance. In particular, PEPP shows greater number of pairs within the cutoff distance with respect to the other polymers, especially at lower states of charge. The larger number of pairs is consistent with its expected higher density of redox sites enabled by the fewer number of "non-phthalimide atoms" of this polymer. Indeed, PEPP has the largest phthalimide density among the three polymers (Figure S19). This higher density of redox sites translates to a higher number of redox pairs as compared to PMAP and PVBP. We also note that all polymers with state of charge between 0 and 20% show a density of redox-active units in the range of 2.00-3.3 cm⁻³ (Figure S19), a range that is larger than the density estimated for the record-high conductivity polymer PTEO (estimated to be at least 1.75 cm⁻³).¹⁷ Finally, the differences between the polymers in terms of both number of radical pairs and radical density are somewhat attenuated as the state of charge reaches 60% (Figures 5 and S19).

2.6. Electronic Percolation

While the electronic coupling distributions we have just seen provide a measure of the average strength of the electronic couplings between nearby redox units in the system, they are only part of the requirements for effective charge transport. Charge transport between sites that are (close to) immobile is essentially a percolation process. Hence, we now analyze electronic percolation in these systems.

We characterize electronic percolation by computing the Kirchhoff transport index, $K_{\rm T}$, a graph-theoretic metric that is useful to evaluate the overall resistance within an electronic network. 34 $K_{\rm T}$ uses a graph-based formulation of transport in which each graph *vertex* represents a radical site in the condensed-phase morphology (a localized charge transport state), and each graph *edge* represents the electronic coupling between such sites (see Methods for details). The larger $K_{\rm T}$ is, the less *resistive* (and hence more conductive) a network is to electronic percolation.

Figure 6 shows $K_{\rm T}$ for the various systems, from which we can draw the following conclusions. Echoing the structural results, swelling (up to 20%) has a minor impact on $K_{\rm T}$, with the expected effect of lowering $K_{\rm T}$. Consistently with the previous results, we see instead a large impact of the polymer state of charge: when going from 0 to 60% charged states, $K_{\rm T}$ drops by almost an order of magnitude in all cases. Finally, the hierarchy PEPP > PMAP > PVBP emerges between the different polymers, indicating that PEPP gives rise to the least resistive (i.e., most conductive) percolating networks among these polymers.

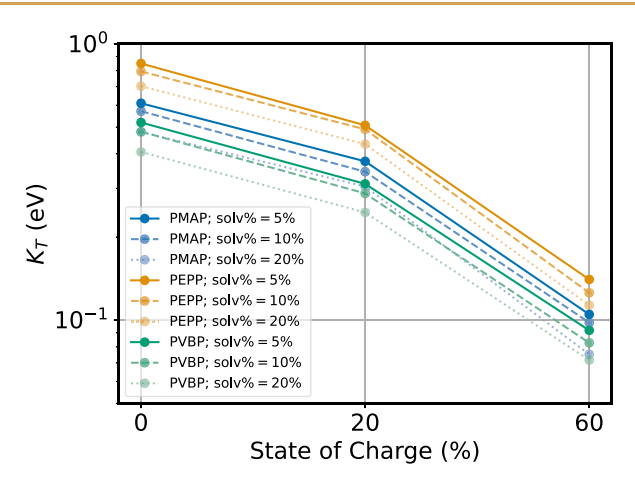


Figure 6. Electronic percolation as a function of state of charge and swelling. Computed Kirchhoff transport index, $K_{\rm T}$, for all the systems. $T = 0.8 \times T_{\rm g}$. Electronic coupling threshold = 100 meV.

Comparing the electronic percolation results of Figure 6 to the phthalimide density noted previously (Figure S19), we note a very strong linear correlation between the two (Figure S20). This strong correlation is due to the coupling strengths being relatively similar between the different systems (Figure 5), leaving the density of radical sites to control $K_{\rm T}$.

2.7. Prediction of Experimental Observables

While the charge transport metric $K_{\rm T}$ is a useful computational metric, it is not an experimental observable. We thus now compute the predicted apparent diffusion coefficient, $D_{\rm app}$, an experimental observable that can be obtained via chronoamperometry or cyclic voltammetry. 21 $D_{\rm app}$ includes electron

diffusion due to electron hopping between redox centers and the physical motion of redox centers; hence, in general $D_{\rm app}$ is given by 35

$$D_{\rm app} = D_{\rm phys} + D_{\rm e} \tag{1}$$

where $D_{\rm phys}$ is the physical diffusion coefficient and $D_{\rm e}$ is the electron-hopping diffusion coefficient. If we assume that Laviron—Andrieux—Savéant theory^{36,37} holds, which is expected to apply for the glassy systems investigated here,²¹ then the apparent kinetics of electron transport is treated as "bounded diffusion" through redox-active pendant groups attached to an immobile backbone. Hence, we have $D_{\rm phys}=0$, and eq 1 reduces to³⁵

$$D_{\rm app} \approx D_{\rm e} = \frac{k_{\rm ex} C_{\rm E} \delta^2}{6} \tag{2}$$

in which $k_{\rm ex}$ is the bimolecular rate constant for electron self-exchange, $C_{\rm E}$ is the concentration of redox species, and δ is the center-to-center distance at electron transfer. $k_{\rm ex}$ is in general given by 35

$$\frac{1}{k_{\rm ex}} = \frac{1}{k_{\rm act}} + \frac{1}{k_{\rm diff}} \approx \frac{1}{k_{\rm act}} \tag{3}$$

where $k_{\rm act}$ is the bimolecular activation-limited rate constant for electron self-exchange, and following ref 35., we assume mean-field conditions and hence neglect the contribution of diffusion ($k_{\rm diff}=0$). Electron hopping between nearby redox centers can be viewed as a Poisson process with the time constant $t_{\rm hop}$ representing the average time between electron hop attempts.³⁵ If so, $t_{\rm hop}$ is related to $k_{\rm act}$ according to

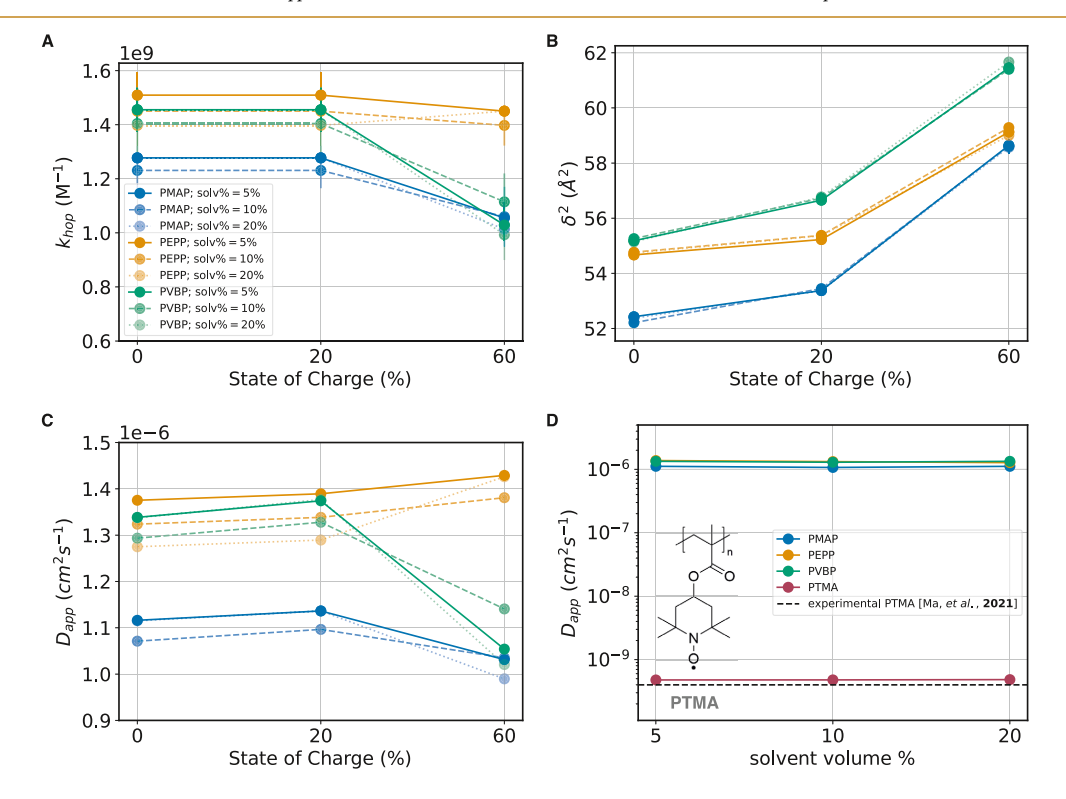


Figure 7. Predicted electron transport performance of systems investigated. (A) Electron self-exchange rate constants (k_{hop}) , (B) squared center-to-center distances at electron transfer (δ^2) , and (C) the resulting predicted Laviron–Andrieux–Savéant apparent diffusion coefficients (D_{app}) , via eq 6). (D) Comparison of predictions of D_{app} for the phthalimide-containing polymers and for a reference nitroxide radical-based polymer PTMA and the available experimental data for PTMA from ref 42.

$$k_{\text{act}} = \frac{1}{t_{\text{hop}} C_{\text{E}}} = \frac{k_{\text{hop}}}{C_{\text{E}}} \tag{4}$$

where k_{hop} is the bimolecular hopping rate for electron self-exchange that can be computed via Marcus—Hush theory^{38–40}

$$k_{\text{hop}} = \left(\frac{\pi}{\lambda k_{\text{B}} T}\right)^{1/2} \left(\frac{V_{ij}^2}{\hbar}\right) \exp\left(-\frac{(\Delta G_0 + \lambda)^2}{4\lambda k_{\text{B}} T}\right)$$
(5)

in which V_{ij} is the electronic coupling between two redox sites, λ is the reorganization energy, ΔG_0 is the standard free energy of the reaction, $k_{\rm B}$ is the Boltzmann constant, and T is the temperature. For our case, the case of self-exchange reactions, $\Delta G_0 = 0.41$ Using eqs 2–4, we arrive at the following, which we can use to estimate $D_{\rm app}$

$$D_{\text{app}} \approx D_{\text{e}} = \frac{k_{\text{ex}} C_{\text{E}} \delta^2}{6} = \frac{k_{\text{act}} C_{\text{E}} \delta^2}{6} = \frac{k_{\text{hop}} \delta^2}{6}$$
(6)

We can readily obtain all the other parameters needed for eq 6 from our simulations: k_{hop} from the mean of the electronic coupling distributions of Figure 5 and computed λ values (reported in Table S2; see also Methods) and δ as an electronic coupling-weighted mean distance ($\delta = \sum_n V_n x_n / \sum_n V_n$, where V_n is the electronic coupling V_{ij} and x_n is the r_{ij} distance for the n-th phthalimide pair; see Figures S24—S26 for plots of the raw data).

The k_{hop} and δ parameters needed to compute D_{app} are shown in Figure 7A-C for all the systems, along with the resulting D_{app} . We note the following: (1) PEPP and PVBP show the largest k_{hop} values; PVBP's relatively low electronic coupling strengths (Figure 5) are compensated by PVBP monomer's showing the lowest inner λ among the polymers (Figure S27); instead, PMAP monomer's largest inner λ among the three backbones offsets the effect of PMAP's highest electronic coupling strengths (Figure 5); (2) k_{hop} values for PMAP and PVBP decrease when going from 20 and 60% state of charge, while they remain constant for PEPP, following the behavior of electronic coupling distributions (Figure 5); (3) δ values are smallest for PMAP, which is thus found to be able to pack phthalimide units at the shortest distances, even surpassing PEPP despite PEPP's largest density of radical sites (Figure S19); this is likely due to the short backbone-phthalimide linker in PEPP not allowing for phthalimide units to pack as good as in the case of PMAP, which corroborates the observed lower amount of face-on configurations in PEPP; (4) PVBP shows the largest δ , which is consistent with PVBP possessing the bulkiest monomer among the investigated polymers; importantly, given that these larger δ values are not accompanied by large decreases in V_{ii} (Figure 5), large δ values are a positive feature in terms of electronic transport for PVBP because they allow this polymer to effectively transport electrons over larger distances with each hopping step, hence favoring D_{app} ; (5) the impact of the polymer state of charge echoes what we have seen so far by overall leading to larger δ and lower $k_{
m hop}$ and consequently lower D_{app} values; however, the effects of the state of charge on δ and k_{hop} compensate each other and result in a decrease of the impact of the state of charge on D_{app} ; we note that experimentally D_{app} at different states of charge cannot be probed; and solvent swelling has, again, a small impact overall; and (6) these factors combined via eq 2 results in the following D_{app} ranking: PEPP > PVBP > PMAP. In summary, the low

inner reorganization energy (molecular-level property) and relatively large effective electron-hopping distance (condensed-phase property) rank PVBP unexpectedly high in terms of electron transport capabilities, while the robustness to structural disorder (introduced by state of charge) and a good balance of inner reorganization energy and electronic coupling strength make PEPP the polymer with the expected largest electron transport capabilities.

We note that the predicted $D_{\rm app}$ (on the order of $10^{-6}~{\rm cm}^2$ s⁻¹, Figure 7) are larger than literature values for the wellstudied poly(TEMPO methacrylate), PTMA, system in the solid state ($\approx 10^{-10}$ cm² s⁻¹, see Table S3) . 20,24,42,43 Since experimental data on the newly proposed polymers are unavailable, to validate our computational approach we computed $D_{\rm app}$ for a PTMA-based solid-state system for which detailed experimental data are available. ⁴² In particular, Ma et al. measured a $D_{\rm app}$ of $4.0 \times 10^{-10}~{\rm cm^2~s^{-1}}$ for the PTMA in H₂O/TEABF₄ at a nitroxide radical concentration of 3.7 M (Table S3). 42 We model this PTMA in H₂O/TEABF₄ system with the same protocol used for the phthalimide-containing polymers (see Figure S29 and Table S4; we note that the 3.7 M concentration corresponds to a swelling of about 10%). For swellings between 5 and 20%, we obtain a $D_{\rm app}$ of 4.8 \times 10⁻¹⁰ cm² s⁻¹, which falls close to the experimental value (Figure 7D). This result validates the multiscale model developed in this work to connect the molecular to the macroscopic picture for the prediction of electronic properties of this class of RAPs.

Comparing the predicted $D_{\rm app}$ values for the phthalimide-based polymers to the predicted $D_{\rm app}$ value for PTMA, we predict an increase of more than 3 orders of magnitude (Figure 7D). The larger D_{app} values for the phthalimide polymers are due to predicted k_{hop} values ($\approx 10^9 \text{ s}^{-1}$) that are larger than PTMA's ($\approx 10^5 \text{ s}^{-1}$, Table S4). The k_{hop} is controlled by the values of λ and V_{ii} , both of which are much improved in the phthalimide-containing polymers proposed here. Regarding λ , as already reported,²⁷ TEMPO exhibits an anomalously high inner reorganization energy, and unsurprisingly, this holds true also for the PTMA monomer ($\lambda_{in} = 0.993 \text{ eV}$), which is about 65% larger than any of the λ_{in} of the phthalimide-containing monomers, see Table S2. Regarding V_{ii} , PTMA exhibits mean electronic couplings of 8 meV in the solid state (Figure S29C), a value which is 4-5 times smaller than the values we find for the phthalimide-containing polymers (43–30 meV, Figure 5). Accordingly, the relatively high electronic couplings that the phthalimide-containing polymers are found to achieve in the solid-state combined with a relatively low inner reorganization energy are responsible for the very high electron transport capabilities predicted here.

3. CONCLUSIONS

We computationally investigated structural, ionic, and electronic properties of phthalimide-based polymers for applications as solid-state n-type materials for all-organic batteries. We assessed the impact of the polymer state of charge, swelling, and backbone chemistry on such solid-state properties. Simulations revealed that the polymer state of charge significantly affects the material's structural, ionic, and electronic properties. While structural properties are robust to swellings up to 20% electrolyte solution volume, an increase in the polymer state of charge leads to a decrease in phthalimide—phthalimide face-on configurations, which in turn decreases electronic couplings. Increases in state of charge and swelling are both found to increase ionic diffusivity due to the decrease

in the systems' $T_{\rm g}$ they imply. Importantly, by combining information from several length scales, our multiscale approach allows us to bridge the gap between bottom-up molecular characteristics and macroscopic properties such as the $D_{\rm app}$. Prediction of D_{app} for the well-studied, reference polymer PTMA allows us to validate our approach, which we then use to rank the phthalimide-containing polymers based on their electron transport capabilities. The low inner reorganization energy (molecular-level property) and relatively large effective electron-hopping distance (condensed-phase property) rank the polystyrene-based polymer PVBP unexpectedly high in terms of electron transport capabilities, while the robustness to structural disorder (introduced by state of charge) and a good balance of inner reorganization energy and electronic coupling strength achieved in the solid state make the poly(ethylene oxide)-based polymer PEPP the one with the predicted largest electron transport capabilities. Overall, due to high electronic couplings achieved in the solid state and relatively low inner reorganization energies, the investigated phthalimide-containing polymers are found to be very promising electron transport materials, with predicted $D_{\rm app}$ on the order of $10^{-6}~{\rm cm^2~s^{-1}}$, which is 3 orders of magnitude larger than $D_{\rm app}$ coefficients for the reference, nitroxide radical-based polymer PTMA.

The multiscale approach developed herein allows for atomistically detailed computational investigations of RAP candidates. As such, the protocol can be used to probe the impact of different electrolytes (which, for example, have been recently found to affect the material capacity by as much as $1000\%^{31}$), different or differently substituted redox units, and other molecular engineering targets, delivering predictions of experimental observables such as $D_{\rm app}$. Future work will also include extension to coarse-grained scales by resorting to recently developed electronic coarse-grained modeling schemes, ^{44,45} opening the way to the study and prediction of processes at large spatiotemporal scales, such as molecular diffusion during cyclic voltammetry, and electronic transport over large-scale molecularly detailed samples.

4. METHODS

4.1. Atomistic Models

All polymers contain 30 repeat units and are terminated by methyl groups. Initial OPLS-AA/CM1A force field parameters for the polymers and the DME solvent were obtained from LigParGen. 46,47 We use $1.20 \times q_{\rm CMS}$ charges, ⁴⁸ that are compatible with OPLS-AA as validated in ref 49. to model the excess charge gained by each phthalimide unit upon reduction. In particular, each charge in a charged phthalimide monomer is computed as follows: $q_i^{\rm red} = q_i^{\rm CMIA,neu} + (q_i^{\rm CMS,red} - q_i^{\rm CMS,neu})$. For PTMA, we used an OPLS-AA/CM1Abased force field from our previous work,⁴⁴ available via Polyply.⁵⁰ We used the TIP3P⁵¹ water model for the swollen PTMA simulations. We modeled TBA+, PF₆-, TEA+, and BF₄- via OPLS-AA-based models available in the literature. ^{52,53} Following the recent systematic study of Doherty et al., 53 we used a molecular charge scaling factor of $0.8 \times q$ for all the charged species (cations, anions, and the charged monomers within a polymer), an effective approach that has recently emerged to correct for the polarization and charge transfer effects that are missing in fixed-charge atomistic force fields. S3 Topologies for all the polymers were built via Polyply.⁵⁰ The charged polymer sequences are generated randomly using the polyply gen_seq tool⁵⁰ first, that generates a JSON file with a random sequence for each of the 100 chains; and those files are then used to generate the polymer topology file via polyply gen params.

4.2. Molecular Dynamics Simulations

Starting configurations for all systems were prepared via Polyply.⁵⁰ All 27 systems (3× polymers, 9× swelling, and state of charge conditions) were equilibrated at 900 K for at least 100 ns-a time that allowed for polymer chain relaxation, as assessed by determining when the end-toend vector autocorrelation function reached a value below 0.1. Snapshots extracted after 100, 150, and 200 ns at 900 K were then cooled down to 100 K (cooling rate = 10 K/ns). Density data obtained during the cooling simulations were used to determine the glass-transition temperature, $T_{\rm g}$, by fitting the low-temperature (glassy) regime and high-temperature (melt) regime linearly as described in detail in the Supporting Information. The obtained $T_{\rm g}$ values are shown in Figure S1. From the cooling trajectories, snapshots at $T_g = 0.8 \times T_{g'}$, $T_g = 1.2 \times T_{g'}$ and 300 K were extracted and relaxed further at those temperature for 100 ns. We used the Verlet scheme with a nonbonded cutoff of 1.1 nm, dispersion corrections, and the particle mesh Ewald method for long-range electrostatics. A time step of 1 fs was used while bonds involving hydrogens were constrained via the LINCS algorithm. Temperature and pressure control was done via a Nosé-Hoover thermostat and a Parrinello-Rahman barostat (coupling parameters, τ_P , of 1 and 5 ps, respectively); and a Berendsen barostat was used for equilibration purposes ($\tau_{\rm p}$ = 1 ps). All molecular dynamics simulations were run with Gromacs version 2021.x or higher.54

4.3. Molecular Configuration Analysis

The configurational maps shown in Figure 3B (and Figures S9, S10) were obtained with the following steps: (i) phthalimide pairs were collected if $r_{ij} \leq 10$ Å; (ii) for the selected pairs, other geometrical descriptors (e.g., θ_{ij}), were computed; (iii) two-dimensional maps were computed by binning the pairs according to their (r_{ij}, θ_{ij}) values; and (iv) the maps were normalized by the volume and the number of ij pairs (see Figure S11). The procedure is implemented in custom Python scripts that make use of the MDAnalysis library. 55,56

4.4. Electronic Structure Calculations

4.4.1. Electronic Coupling Calculations. We used orbital overlaps as a proxy for the electronic couplings. We computed orbital overlaps as done in our recent work via Gaussian (version C.01) and Multiwfn wb97X-D/def2-SV(P) level of theory. Orbital overlaps were computed between the least unoccupied molecular orbital (LUMO) of the neutral species and the singly occupied molecular orbital (SOMO) of the radical anion in the case of N-methyl-phthalimide $\langle \phi_{\rm LUMO} | \phi_{\rm SOMO} \rangle$ and the SOMO of the neutral radical and the LUMO of the cation, $\langle \phi_{\rm SOMO} | \phi_{\rm LUMO} \rangle$ in the case of TEMPO. Reference electronic couplings were computed with the DImer PROjection (DIPRO) method as implemented in CATNIP (a code recently used for mixed ionic-electronic conductors of the orbital overlap calculations were used.

4.4.2. Reorganization Energy Calculations. All the calculations were performed using Gaussian16 (version C.01)^{S7} at the ω B97X-D/def2-SV(P) level of theory with the implicit DME solvent using the polarizable continuum model. The reorganization energy, λ , can be expressed as the sum of inner and outer reorganization energy, $\lambda_{\rm in}$ and $\lambda_{\rm out}$ separately. With Nelsen's four-point method, 61 $\lambda_{\rm in}$ can be estimated via

$$\lambda_{\rm in} = (E_{\rm neu}^{\rm red} + E_{\rm red}^{\rm neu}) - (E_{\rm neu}^{\rm neu} + E_{\rm red}^{\rm red})$$
 (7)

where E represents the single-point energy of a molecule calculated at a redox state specified in superscript under the geometry optimized at a redox state specified in subscript. $\lambda_{\rm out}$ can be further estimated based on the simplified model given by Marcus³⁸

$$\lambda_{\text{out}} = (\Delta e)^2 \left(\frac{1}{2r_{\text{D}}} + \frac{1}{2r_{\text{A}}} + \frac{1}{R_{\text{DA}}} \right) \left(\frac{1}{n^2} - \frac{1}{\epsilon_{\text{r}}} \right)$$
 (8)

where Δe is the amount charge being transferred ($\Delta e = 1$), $r_{\rm D}$ and $r_{\rm A}$ are the respective donor and acceptor radii, respectively, $R_{\rm DA}$ is the value of donor/acceptor separation, and n and $\varepsilon_{\rm r}$ are the refractive

JACS Au pubs.acs.org/jacsau Article

index and the static dielectric constant, respectively. $\varepsilon_{\rm r}$ is determined as a mixture of the dielectric constant of the polymer and the dielectric constant of the solvent as shown in Figure S27. Donor and acceptor radii, being same for the phthalimide unit, were estimated from the Universal Force Field radii using Gaussian16 (namely, $r_{\rm D}=r_{\rm A}=3.740$ Å for N-methyl-phthalimide and $r_{\rm D}=r_{\rm A}=3.942$ for TEMPO). We estimated $R_{\rm DA}$ by assuming it equals $r_{\rm D}+r_{\rm A}$ at the closest approach. Note that eq. 8 is in atomic units.

4.5. Surrogate Machine Learning Models

4.5.1. Data Sets. Training data for the machine learning models (neural networks, see below) were generated with a procedure similar to our previous work ⁴⁴ but using a condensed phase of monomers (N-methyl-phthalimide or TEMPO) instead of the polymers. Namely, we sampled phthalimide pair configurations from a condensed phase simulation of pure phthalimide sampled at temperatures between 600 and 300 K; we extract \approx 15, at intervals of 10 K between the two temperatures, and from each snapshot we extract \approx 1000 pairs, leading to a total data set size of over 146 343 data points. The same was done for TEMPO, leading to a total data set size of 147 804 data points in that case.

4.5.2. Input Representation, Model, and Training Details. As done in our previous work,44 we trained feed-forward artificial neural networks using the conformations (in the form of a reciprocal distance matrix) as input and the orbital overlaps as labels. In particular, for each pair conformation a reciprocal distance matrix D between all atoms was computed. Its elements are $D_{kl}^{(i,j)} = |\mathbf{r}_k^{(i)} - \mathbf{r}_l^{(j)}|^{-1}$ where **r** is the position vector, *i* and *j* are the monomer indices, and k and l are the atom indices. Each matrix was flattened and the resulting one-dimensional vector (of dimension N^2 , with N = 12 for N-methyl-phthalimide and N = 11 for TEMPO) was used as the input feature for the supervised machine learning task. The base 10 logarithm of $\langle \phi_{\text{SOMO}} | \phi_{\text{LUMO}} \rangle$ was employed to assess orbital overlaps. To ensure flexibility, a fully connected, feed-forward neural network was utilized, comprising an input layer of dimension M, followed by four batch-normalized hidden layers, each with the same number of neurons. M is the dimension of the flattened input vector and is hence equal to N^2 . Hyperparameters, including the number of neurons in hidden layers, batch size, and training epochs, were optimized. Training utilized the default learning rate of the NAdam optimizer (0.001) and standard scaling was applied to input and output features. 10% of each data set was reserved for testing (holdout data set), while the remaining data points were used for training and validation through 5-fold cross-validation. Hyperparameters were fine-tuned via grid search using 5-fold cross-validated performance. The model's final performance was evaluated by applying the best-performing model, as determined by 5-fold crossvalidation, to the held-out test set. The results on the test set are shown on Figure S17. The surrogate models were implemented using the Keras⁶² and scikit-learn⁶³ libraries.

4.6. Graph-Theoretic Approach to Percolation

To quantify electronic percolation capabilities of the systems, we use the Kirchhoff transport index, $K_{\rm T}$. 34 $K_{\rm T}$ corresponds to the summation of inverse resistances of all paths between any two points in a graph that represents the charge transport network, normalized by the total number of pathways $\frac{1}{2}N^2$. $K_{\rm T}$ is computed as follows: we first computed the weighted adjacency matrix, **A**, with elements

$$A_{ij} = \begin{cases} \begin{vmatrix} V_{ij} & \text{if } i \neq j \\ 0 & \text{if } i = j \end{cases}$$

$$(9)$$

was computed for each morphology, where V_{ij} is the electronic coupling between sites i and j. A is used to construct the admittance matrix, Λ , whose elements, Λ_{ij} , correspond to the admittance between each site, that is, the inverse of the effective resistance. For more details, we refer to the original $K_{\rm T}$ work. 34 $K_{\rm T}$ is then finally calculated as

$$K_{\rm T} = \frac{1}{2N^2} \sum_{i,j} \Lambda_{ij} \tag{10}$$

in which we note that, to avoid double counting of Λ_{ip} we normalize by $2N^2$ (instead of N^2 as done in ref 34). We use a threshold of 100 meV to define if a pair is coupled or not in Figure 6. We note however that the analysis is very robust to different values of this threshold, as shown in Figure S21. Moreover, Figures S22, S23 show the number of networks and network sizes as a function of the threshold, respectively. We use the kugupu Python package to compute $K_{\rm T}$. ⁶⁴

ASSOCIATED CONTENT

Data Availability Statement

Models, code, and data associated with this work are available at https://github.com/ricalessandri/redox-active-polymers. All polymer models have been implemented in the Polyply⁵⁰ library and are available at https://github.com/marrink-lab/polyply_1.0. Simulation workflows and data generated will be made available via CRIPT.⁶⁵

Supporting Information

The Supporting Information is available free of charge at https://pubs.acs.org/doi/10.1021/jacsau.4c00276.

 $T_{\rm g}$ calculation details and additional $T_{\rm g}$ results; number of molecules contained in each system; schematic of the atomistic molecular dynamics protocol; additional RDFs and configurational maps; intramolecular vs intramolecular pair breakdown; electronic coupling correlations (overlap vs electronic couplings and DFT overlaps vs neural network-predicted overlaps); additional electronic percolation results; phthalimide interdistance vs overlap heatmaps; reorganization energies; and additional $D_{\rm app}$ results (PDF)

AUTHOR INFORMATION

Corresponding Authors

Daniel P. Tabor — Department of Chemistry, Texas A&M University, College Station, Texas 77842, United States; orcid.org/0000-0002-8680-6667; Email: daniel_tabor@tamu.edu

Juan J. de Pablo — Pritzker School of Molecular Engineering, University of Chicago, Chicago, Illinois 60637, United States; ⊚ orcid.org/0000-0002-3526-516X; Email: depablo@uchicago.edu

Authors

Riccardo Alessandri — Pritzker School of Molecular Engineering, University of Chicago, Chicago, Illinois 60637, United States; Oorcid.org/0000-0003-1948-5311

Cheng-Han Li − Department of Chemistry, Texas A&M University, College Station, Texas 77842, United States; orcid.org/0000-0002-1095-1593

Sheila Keating — Department of Chemistry, University of Chicago, Chicago, Illinois 60637, United States;
occid.org/0000-0002-8189-1073

Khirabdhi T. Mohanty — Artie McFerrin Department of Chemical Engineering, Texas A&M University, College Station, Texas 77843, United States

Aaron Peng — Pritzker School of Molecular Engineering, University of Chicago, Chicago, Illinois 60637, United States Jodie L. Lutkenhaus — Artie McFerrin Department of Chemical Engineering and Department of Materials Science & Engineering, Texas A&M University, College Station, Texas 77843, United States; o orcid.org/0000-0002-2613-6016

Stuart J. Rowan — Pritzker School of Molecular Engineering, University of Chicago, Chicago, Illinois 60637, United States; Department of Chemistry, University of Chicago, Chicago, Illinois 60637, United States; orcid.org/0000-0001-8176-0594

Complete contact information is available at: https://pubs.acs.org/10.1021/jacsau.4c00276

Notes

The authors declare no competing financial interest.

ACKNOWLEDGMENTS

This research was supported by grant NSF-DMR-2119672/2119673 funded by the National Science Foundation. R.A. acknowledges support by the Dutch Research Council (NWO Rubicon 019.202EN.028). The authors acknowledge the Research Computing Center of the University of Chicago for computational resources. Portions of this research were conducted with the advanced computing resources provided by Texas A&M High Performance Research Computing.

REFERENCES

- (1) Tan, Y.; Hsu, S.-N.; Tahir, H.; Dou, L.; Savoie, B. M.; Boudouris, B. W. Electronic and Spintronic Open-Shell Macromolecules, Quo Vadis? *J. Am. Chem. Soc.* **2022**, *144*, 626–647.
- (2) Nishide, H. Organic redox polymers as electrochemical energy materials. *Green Chem.* **2022**, *24*, 4650–4679.
- (3) Wang, S.; Easley, A. D.; Lutkenhaus, J. L. 100th Anniversary of Macromolecular Science Viewpoint: Fundamentals for the Future of Macromolecular Nitroxide Radicals. *ACS Macro Lett.* **2020**, *9*, 358–370.
- (4) Janoschka, T.; Hager, M. D.; Schubert, U. S. Powering up the Future: Radical Polymers for Battery Applications. *Adv. Mater.* **2012**, 24, 6397–6409.
- (5) Kim, J.; Kim, J. H.; Ariga, K. Redox-Active Polymers for Energy Storage Nanoarchitectonics. *Joule* **2017**, *1*, 739–768.
- (6) Ji, L.; Shi, J.; Wei, J.; Yu, T.; Huang, W. Air-Stable Organic Radicals: New-Generation Materials for Flexible Electronics? *Adv. Mater.* **2020**, 32, 1908015.
- (7) Hager, M. D.; Esser, B.; Feng, X.; Schuhmann, W.; Theato, P.; Schubert, U. S. Polymer-Based Batteries—Flexible and Thin Energy Storage Systems. *Adv. Mater.* **2020**, *32*, 2000587.
- (8) Esser, B.; Dolhem, F.; Becuwe, M.; Poizot, P.; Vlad, A.; Brandell, D. A perspective on organic electrode materials and technologies for next generation batteries. *J. Power Sources* **2021**, *482*, 228814.
- (9) Goujon, N.; Casado, N.; Patil, N.; Marcilla, R.; Mecerreyes, D. Organic batteries based on just redox polymers. *Prog. Polym. Sci.* **2021**, *122*, 101449.
- (10) Nguyen, T. P.; Easley, A. D.; Kang, N.; Khan, S.; Lim, S.-M.; Rezenom, Y. H.; Wang, S.; Tran, D. K.; Fan, J.; Letteri, R. A.; He, X.; Su, L.; Yu, C.-H.; Lutkenhaus, J. L.; Wooley, K. L. Polypeptide organic radical batteries. *Nature* **2021**, *593*, *61*–*66*.
- (11) Easley, A. D.; Ma, T.; Lutkenhaus, J. L. Imagining circular beyond lithium-ion batteries. *Joule* **2022**, *6*, 1743–1749.
- (12) Rohland, P.; Schröter, E.; Nolte, O.; Newkome, G. R.; Hager, M. D.; Schubert, U. S. Redox-active polymers: The magic key towards energy storage a polymer design guideline progress in polymer science. *Prog. Polym. Sci.* **2022**, *125*, 101474.
- (13) Esser, B. Redox polymers as electrode-active materials for batteries. *Org. Mater.* **2019**, *01*, 063–070.
- (14) Chi, T.; Akkiraju, S.; Liang, Z.; Tan, Y.; Kim, H. J.; Zhao, X.; Savoie, B. M.; Boudouris, B. W. Design of an n-type low glass transition temperature radical polymer. *Polym. Chem.* **2021**, *12*, 1448–1457.

- (15) Li, M.; Rhodes, Z.; Cabrera-Pardo, J. R.; Minteer, S. D. Recent advancements in rational design of non-aqueous organic redox flow batteries. *Sustainable Energy Fuels* **2020**, *4*, 4370–4389.
- (16) Casado, N.; Mantione, D.; Shanmukaraj, D.; Mecerreyes, D. Symmetric All-Organic Battery Containing a Dual Redox-Active Polymer as Cathode and Anode Material. *ChemSusChem* **2020**, *13*, 2464–2470.
- (17) Joo, Y.; Agarkar, V.; Sung, S. H.; Savoie, B. M.; Boudouris, B. W. A nonconjugated radical polymer glass with high electrical conductivity. *Science* **2018**, *359*, 1391–1395.
- (18) Paulsen, B. D.; Tybrandt, K.; Stavrinidou, E.; Rivnay, J. Organic mixed ionic—electronic conductors. *Nat. Mater.* **2020**, *19*, 13–26.
- (19) Keene, S. T.; Gueskine, V.; Berggren, M.; Malliaras, G. G.; Tybrandt, K.; Zozoulenko, I. Exploiting mixed conducting polymers in organic and bioelectronic devices. *Phys. Chem. Chem. Phys.* **2022**, 24, 19144–19163.
- (20) Wang, S.; Li, F.; Easley, A. D.; Lutkenhaus, J. L. Real-time insight into the doping mechanism of redox-active organic radical polymers. *Nat. Mater.* **2019**, *18*, 69–75.
- (21) Ma, T.; Easley, A. D.; Thakur, R. M.; Mohanty, K. T.; Wang, C.; Lutkenhaus, J. L. Nonconjugated Redox-Active Polymers: Electron Transfer Mechanisms, Energy Storage, and Chemical Versatility. *Annu. Rev. Chem. Biomol. Eng.* **2023**, *14*, 187–216.
- (22) Oyaizu, K.; Nishide, H. Radical Polymers for Organic Electronic Devices: A Radical Departure from Conjugated Polymers? *Adv. Mater.* **2009**, *21*, 2339–2344.
- (23) Kemper, T. W.; Larsen, R. E.; Gennett, T. Relationship between Molecular Structure and Electron Transfer in a Polymeric Nitroxyl-Radical Energy Storage Material. *J. Phys. Chem. C* **2014**, *118*, 17213–17220.
- (24) Sato, K.; Ichinoi, R.; Mizukami, R.; Serikawa, T.; Sasaki, Y.; Lutkenhaus, J.; Nishide, H.; Oyaizu, K. Diffusion-Cooperative Model for Charge Transport by Redox-Active Nonconjugated Polymers. *J. Am. Chem. Soc.* **2018**, *140*, 1049–1056.
- (25) Stumme, N.; Perera, A. S.; Horvath, A.; Ruhunage, S.; Duffy, D. H.; Koltonowski, E. M.; Tupper, J.; Dzierba, C.; McEndaffer, A. D.; Teague, C. M.; Risko, C.; Shaw, S. K. Probing Redox Properties of Extreme Concentrations Relevant for Nonaqueous Redox-Flow Batteries. ACS Appl. Energy Mater. 2023, 6, 2819–2831.
- (26) Bello, L.; Sing, C. E. Mechanisms of Diffusive Charge Transport in Redox-Active Polymer Solutions. *Macromolecules* **2020**, 53, 7658–7671.
- (27) Tan, Y.; Casetti, N. C.; Boudouris, B. W.; Savoie, B. M. Molecular Design Features for Charge Transport in Nonconjugated Radical Polymers. *J. Am. Chem. Soc.* **2021**, *143*, 11994–12002.
- (28) Li, C.-H.; Tabor, D. P. Discovery of lead low-potential radical candidates for organic radical polymer batteries with machine-learning-assisted virtual screening. *J. Mater. Chem. A* **2022**, *10*, 8273–8282.
- (29) Duke, R.; Bhat, V.; Sornberger, P.; Odom, S. A.; Risko, C. Towards a comprehensive data infrastructure for redox-active organic molecules targeting non-aqueous redox flow batteries. *Digital Discovery* **2023**, *2*, 1152–1162.
- (30) Tan, Y.; Boudouris, B. W.; Savoie, B. M. Bridging the Monomer to Polymer Gap in Radical Polymer Design. *ACS Macro Lett.* **2023**, 12, 801–807.
- (31) Ma, T.; Li, C.-H.; Thakur, R. M.; Tabor, D. P.; Lutkenhaus, J. L. The role of the electrolyte in non-conjugated radical polymers for metal-free aqueous energy storage electrodes. *Nat. Mater.* **2023**, *22*, 495–502.
- (32) Troisi, A.; Orlandi, G. Band Structure of the Four Pentacene Polymorphs and Effect on the Hole Mobility at Low Temperature. *J. Phys. Chem. B* **2005**, *109*, 1849–1856.
- (33) Baumeier, B.; Kirkpatrick, J.; Andrienko, D. Density-functional based determination of intermolecular charge transfer properties for large-scale morphologies. *Phys. Chem. Chem. Phys.* **2010**, *12*, 11103–11113.

- (34) Jackson, N. E.; Savoie, B. M.; Chen, L. X.; Ratner, M. A. A. A Simple Index for Characterizing Charge Transport in Molecular Materials. *J. Phys. Chem. Lett.* **2015**, *6*, 1018–1021.
- (35) Blauch, D. N.; Saveant, J. M. Dynamics of electron hopping in assemblies of redox centers. Percolation and diffusion. *J. Am. Chem. Soc.* **1992**, *114*, 3323–3332.
- (36) Laviron, E.; Roullier, L.; Degrand, C. A multilayer model for the study of space distributed redox modified electrodes: Part II. Theory and application of linear potential sweep voltammetry for a simple reaction. *J. Electroanal. Chem. Interfacial Electrochem.* 1980, 112. 11–23.
- (37) Andrieux, C. P.; Savéant, J. Electron transfer through redox polymer films. J. Electroanal. Chem. Interfacial Electrochem. 1980, 111, 377–381.
- (38) Marcus, R. A. On the Theory of Oxidation-Reduction Reactions Involving Electron Transfer. I. J. Chem. Phys. 1956, 24, 966–978.
- (39) Marcus, R.; Sutin, N. Electron transfers in chemistry and biology. *Biochim. Biophys. Acta* 1985, 811, 265–322.
- (40) Hush, N. Electron transfer in retrospect and prospect: 1: Adiabatic electrode processes. J. Electroanal. Chem. 1999, 460, 5–29.
- (41) Marcus, R. A. Electron Transfer Reactions in Chemistry: Theory and Experiment (Nobel Lecture). *Angew. Chem., Int. Ed.* **1993**, 32, 1111–1121.
- (42) Ma, T.; Easley, A. D.; Wang, S.; Flouda, P.; Lutkenhaus, J. L. Mixed electron-ion-water transfer in macromolecular radicals for metal-free aqueous batteries. *Cell Rep. Phys. Sci.* **2021**, *2*, 100414.
- (43) Tokue, H.; Murata, T.; Agatsuma, H.; Nishide, H.; Oyaizu, K. Charge—Discharge with Rocking-Chair-Type Li+ Migration Characteristics in a Zwitterionic Radical Copolymer Composed of TEMPO and Trifluoromethanesulfonylimide with Carbonate Electrolytes for a High-Rate Li-Ion Battery. *Macromolecules* 2017, 50, 1950—1958.
- (44) Alessandri, R.; de Pablo, J. J. Prediction of Electronic Properties of Radical-Containing Polymers at Coarse-Grained Resolutions. *Macromolecules* **2023**, *56*, 3574–3584.
- (45) Maier, J. C.; Jackson, N. E. Bypassing Backmapping: Coarse-Grained Electronic Property Distributions Using Heteroscedastic Gaussian Processes. J. Chem. Phys. 2022, 157, 174102.
- (46) Jorgensen, W. L.; Tirado-Rives, J. Potential energy functions for atomic-level simulations of water and organic and biomolecular systems. *Proc. Natl. Acad. Sci. U.S.A.* **2005**, *102*, *6665–6670*.
- (47) Dodda, L. S.; Cabeza de Vaca, I.; Tirado-Rives, J.; Jorgensen, W. L. LigParGen web server: an automatic OPLS-AA parameter generator for organic ligands. *Nucleic Acids Res.* **2017**, *45*, W331–W336
- (48) Marenich, A. V.; Jerome, S. V.; Cramer, C. J.; Truhlar, D. G. Charge Model 5: an Extension of Hirshfeld Population Analysis for the Accurate Description of Molecular Interactions in Gaseous and Condensed Phases. *J. Chem. Theory Comput.* **2012**, *8*, 527–541.
- (49) Dodda, L. S.; Vilseck, J. Z.; Cutrona, K. J.; Jorgensen, W. L. Evaluation of CM5 Charges for Nonaqueous Condensed-Phase Modeling. *J. Chem. Theory Comput.* **2015**, *11*, 4273–4282.
- (50) Grünewald, F.; Alessandri, R.; Kroon, P. C.; Monticelli, L.; Souza, P. C. T.; Marrink, S. J. Polyply; a python suite for facilitating simulations of macromolecules and nanomaterials. *Nat. Commun.* **2022**, *13*, 68.
- (51) Jorgensen, W. L.; Chandrasekhar, J.; Madura, J. D.; Impey, R. W.; Klein, M. L. Comparison of simple potential functions for simulating liquid water. *J. Chem. Phys.* **1983**, *79*, 926–935.
- (52) Canongia Lopes, J. N.; Pádua, A. A. H. Molecular Force Field for Ionic Liquids Composed of Triflate or Bistriflylimide Anions. *J. Phys. Chem. B* **2004**, *108*, 16893–16898.
- (53) Doherty, B.; Zhong, X.; Gathiaka, S.; Li, B.; Acevedo, O. Revisiting OPLS Force Field Parameters for Ionic Liquid Simulations. *J. Chem. Theory Comput.* **2017**, *13*, 6131–6145.
- (54) Abraham, M. J.; Murtola, T.; Schulz, R.; Páll, S.; Smith, J. C.; Hess, B.; Lindahl, E. GROMACS: high Performance Molecular Simulations Through Multi-Level Parallelism from Laptops to Supercomputers. *SoftwareX* **2015**, *1*–2, 19–25.

- (55) Michaud-Agrawal, N.; Denning, E. J.; Woolf, T. B.; Beckstein, O. MDAnalysis: a toolkit for the analysis of molecular dynamics simulations. *J. Comput. Chem.* **2011**, 32, 2319–2327.
- (56) Gowers, R. J.; Linke, M.; Barnoud, J.; Reddy, T. J. E.; Melo, M. N.; Seyler, S. L.; Dotson, D. L.; Domanski, J.; Buchoux, S.; Kenney, I. M.; Beckstein, O. MDAnalysis: a Python package for the rapid analysis of molecular dynamics simulations *Proceedings of the 15th Python in Science Conference*; Scipy: Austin, TX, 2016, pp 102–109.
- (57) Frisch, M. J.; Trucks, G. W.; Schlegel, H. B.; Scuseria, G. E.; Robb, M. A.; Cheeseman, J. R.; Scalmani, G.; Barone, V.; Petersson, G. A.; Nakatsuji, H.; Li, X.; Caricato, M.; Marenich, A. V.; Bloino, J.; Janesko, B. G.; Gomperts, R.; Mennucci, B.; Hratchian, H. P.; Ortiz, J. V.; Izmaylov, A. F.; Sonnenberg, J. L.; Williams-Young, D.; Ding, F.; Lipparini, F.; Egidi, F.; Goings, J.; et al. *Gaussian 16*, Revision C.01; Gaussian Inc.: Wallingford CT, 2016.
- (58) Lu, T.; Chen, F. M. Multiwfn: A multifunctional wavefunction analyzer. *J. Comput. Chem.* **2012**, 33, 580–592.
- (59) Brown, J. S. CATNIP (Version 1.9). 2023, https://github.com/ JoshuaSBrown/QC Tools (accessed Oct 31, 2023).
- (60) Rolland, N.; Modarresi, M.; Franco-Gonzalez, J. F.; Zozoulenko, I. Large scale mobility calculations in PEDOT (Poly(3,4-ethylenedioxythiophene)): backmapping the coarse-grained Martini morphology. *Comput. Mater. Sci.* **2020**, *179*, 109678.
- (61) Nelsen, S. F.; Blackstock, S. C.; Kim, Y. Estimation of inner shell Marcus terms for amino nitrogen compounds by molecular orbital calculations. *J. Am. Chem. Soc.* **1987**, *109*, 677–682.
- (62) Chollet, F. Keras. 2015, https://keras.io (accessed Oct 31, 2023).
- (63) Pedregosa, F.; Varoquaux, G.; Gramfort, A.; Michel, V.; Thirion, B.; Grisel, O.; Blondel, M.; Prettenhofer, P.; Weiss, R.; Dubourg, V.; Vanderplas, J.; Passos, A.; Cournapeau, D.; Brucher, M.; Perrot, M.; Edouard, D. Scikit-learn: Machine Learning in Python. *J. Mach. Learn. Res.* **2011**, *12*, 2825–2830.
- (64) Gowers, R.; Matta, M.; Nguyen, H. *Kugupu/Kugupu: v0.1.2.* 2023, https://github.com/kugupu/kugupu/releases (accessed Oct 31, 2023).
- (65) Walsh, D. J.; Zou, W.; Schneider, L.; Mello, R.; Deagen, M. E.; Mysona, J.; Lin, T.-S.; de Pablo, J. J.; Jensen, K. F.; Audus, D. J.; Olsen, B. D. Community Resource for Innovation in Polymer Technology (CRIPT): A Scalable Polymer Material Data Structure. ACS Cent. Sci. 2023, 9, 330–338.